Cross-scale interaction between microturbulence and meso-scale reversed shear Alfvén eigenmodes in DIII-D plasmas

Q1

Q2

P. Liu[1,2,*] ⓘ, **X. Wei**[1] ⓘ, **Z. Lin**[1], **W.W Heidbrink**[1] ⓘ, **G. Brochard**[3], **G.J. Choi**[4] ⓘ, **J.H. Nicolau**[1] ⓘ and **W. Zhang**[2] ⓘ

[1] Department of Physics and Astronomy, University of California, Irvine, CA 92697, United States of America
[2] Institute of Physics, Chinese Academy of Sciences, Beijing 100190, China
[3] ITER organisation, Route de Vinon sur Verdon, CS 90 046 13067, St., Paul Lez Durance, France
[4] Nuclear Research Institute for Future Technology and Policy, Seoul National University, Seoul 08826, Korea, Republic Of

E-mail: pfliu@iphy.ac.cn

CrossMark

Abstract

This paper reports global nonlinear gyrokinetic simulations that couple meso-scale reversed shear Alfvén eigenmodes (RSAEs) driven by energetic particles (EPs) and ion temperature gradient (ITG) microturbulence driven by thermal plasma, using equilibrium and profiles from DIII-D discharge #159243. In simulations focusing only on the ITG, electrostatic ITG drives a huge thermal ion heat transport, which is reduced by a factor of 10 to a level closer to the experimental value in electromagnetic simulation due to finite β effect. In the simulations coupling the RSAE and ITG, ITG can scatter the resonant EP nonlinearly trapped by the RSAE and damp the zonal flows generated by the RSAE. The regulation of the RSAE by the ITG greatly reduces the initial saturation amplitude of the RSAE but increases the RSAE amplitude and associated EP transport to experimental levels in the quasi-steady state. The RSAE effects on the ITG, specifically the stronger zonal flows generated by the RSAE and the RSAE frequency modulation of the ITG-induced thermal ion heat transport, in turn, leads to a reduction of the thermal ion heat transport by more than a factor of 2. For a stronger background ITG, the regulation of the RSAE by the ITG is stronger, while the RSAE effects on the ITG are weaker. This work highlights the importance of cross-scale coupling in the dynamics of the AE turbulence and EP transport.

Keywords: reversed shear Alfvén eigenmodes, microturbulence, cross-scale interaction, global gyrokinetic simulations

Q3 (Some figures may appear in colour only in the online journal)

---

* Author to whom any correspondence should be addressed.

1. Introduction

The confinement of energetic particles (EPs), including fusion products (α-particles) and fast ions produced by auxiliary heating through ion cyclotron radio frequencies (ICRFs) waves or neutral beams injection, is a critical physics issue for achieving high-performance and ignition in magnetic confinement fusion devices [1–4], since the ignition relies on good confinement of α-particles. However, meso-scale Alfvén eigenmodes (AEs) [5–7], driven by strong EP pressure gradient, can result in an anomalous EP transport in the core region that reduces the heating efficiency and prevents the ignition. Therefore, an understanding of AE and associated EP transport is essential for the optimization of existing machines and for the prediction of α-particle confinement in burning fusion plasmas.

In the last two decades, numerical simulations of AE and EP physics have played an important role in verifying the analytic theory and understanding the experiments, thanks to the rapid growth in computation power. Linear simulations have often been performed to identify the modes observed in experiments [8, 9] and their excitation mechanism. Nonlinear simulations have aimed to understand nonlinear wave–wave and wave-particle interactions that lead to mode saturation [10], frequency chirping [11, 12], and fast ion anomalous loss. Due to the constraint of physical model and computation power, however, most simulations [10, 13–18] have focused only on the AE nonlinear dynamics. And they commonly observe a huge initial burst of the AE amplitude followed by a quickly quenched nonlinear phase, leading to uncertainty in comparison with experimental measurements of a quasi-steady state AE. For instance, recent global nonlinear gyrokinetic simulations of the reversed shear AE (RSAE) using equilibrium and plasma profiles from the DIII-D tokamak shot #159243 find that the RSAE amplitude and associated EP transport are much higher than experimental observations at initial nonlinear saturation, but quickly drop to very low levels in nonlinear phase due to the flattening of EP distribution function at resonances, even with EP collisions and multiple toroidal mode coupling effects [18]. This indicates that single scale simulations focusing only on AE could not fully explain the experimental measurements in DIII-D.

Hot magnetized plasmas are highly complex nonlinear systems characterized by multiple temporal and spatial scales, making cross-scale interactions inevitable in physical processes involving different scales. Recent studies [19–28] have suggested the possibility of coupling between thermal plasma and EP, specifically the cross-scale interaction between microscale drift-wave microturbulence and meso-scale AE. The microturbulence [29], with a characteristic length on the order of thermal ion gyroradius and driven by pressure gradients of thermal plasmas, is ubiquitous in all regimes and geometries and leads to anomalous transport of electrons and thermal ions. Despite the spatial and temporal separation, there can be strong cross-scale interactions between the AE and microturbulence. For the effects of microturbulence on AE, CGYRO first reports that the AE saturation needs the zonal flows generated by microturbulence [19]. Later studies show

that microturbulence can affect the zonal flows and structures generated by the AE [21, 30, 31], and scatter the nonlinearly trapped EP, thereby affecting phase space dynamics in the nonlinear AE-EP interaction [22, 24]. Scattering of toroidicity-induced AE (TAE) by microturbulence could also lead to an appreciable damping of TAE due to Landau damping of nonlinearly generated short-wavelength kinetic Alfvén waves quasimodes [27]. For the effects of EP on microturbulence, on the other hand, larger zonal flows can be generated in the presence of EP, resulting in a significant suppression of the turbulence-induced thermal plasma heat transport and enhancement of thermal plasma confinement [23]. Dilution effects due to EP have been found to modify zonal flows, resulting in an enhanced regulation of drift wave turbulence by the zonal flows [32]. Additionally, beta-induced AEs have been shown to drive an electron heat flux as efficiently, or even more efficiently, as the ion temperature gradient (ITG) turbulence [25].

Fully self-consistent simulations of cross-scale interaction must incorporate microturbulence and the AE with the kinetic effects of both EP and thermal plasma. Due to the multiple temporal and spatial scales, global integrated simulation incorporating multiple physical processes in a complex toroidal geometry is a grand challenge for both simulation models and supercomputers. Using the state-of-the-art global gyrokinetic code (GTC) [33], which has been applied to microturbulence [34–40], magnetohydrodynamic instabilities [41, 42] and AE [11, 43, 44], such kind of multiscale simulations become feasible on the world's fastest supercomputers. Recent GTC simulations [28] coupling micro-meso scales find that ITG microturbulence can play a critical role in regulating the AE nonlinear dynamics and associated EP transport in the DIII-D plasma, even though microturbulence directly drives little EP transport due to gyro-averaging effects as expected by conventional wisdom [36, 45–48]. In the presence of background microturbulence, RSAE amplitude and associated EP transport decrease drastically at the initial saturation but later increase to the experimental observation in the quasi-steady state with regular RSAE mode structure. In the quasi-steady state ITG-RSAE turbulence, radial structure and mode amplitude of the RSAE from gyrokinetic simulations, for the first time, agree well with the electron cyclotron emission (ECE) measurement [49]. The electron density fluctuation spectra are consistent with 64-channel beam emission spectroscopy measurements [50] and the estimated effective EP diffusivity and turbulence intensity are close to experimental observations as well.

Building on previous works ([18] and [28]), we report here the nonlinear dynamics of the ITG turbulence, and its detailed cross-scale interaction with the RSAE. We begin with simulations focusing only on the ITG and find that electrostatic ITG drives a huge thermal ion heat transport, which is reduced by a factor of 10 to a level closes to the experimental value in electromagnetic simulation due to finite β effect (β is the ratio between the plasma kinetic and magnetic pressure). We then explore the cross-scale coupling between RSAE and ITG. We find that ITG can scatter the resonant EP nonlinearly trapped by the RSAE, thereby shrinking the phase space coherent

structures formed by resonant particles and restoring the linear EP instability drive. Additionally, ITG reduces the amplitude of zonal structures of thermal species, especially for the long radial wavelength k_r components which are more effective to suppress the RSAE, leading to weaker zonal flow effects on the RSAE in the ITG-RSAE coupled simulation compared with the simulation focusing only on the RSAE. The regulation of the RSAE by the ITG greatly reduces the initial saturation amplitude of RSAE and increases the mode amplitude as well as associated EP transport to the experimental level in the quasi-steady state. The RSAE effects on the ITG include stronger zonal flows in the coupled simulation than in the simulation focusing only on the ITG and the RSAE frequency modulation of the ITG-induced thermal ion heat transport, in turn, results in a reduction of thermal ion heat transport by more than a factor of 2. For a stronger ITG, the regulation of RSAE by ITG is stronger, while the RSAE effects on the ITG are weaker.

This paper is organized as follows. In section 2, we provide an overview of the equilibrium profiles and basic simulation parameters. Section 3 details the nonlinear simulation results of electrostatic and electromagnetic ITG without EP. In section 4, we present simulations coupling ITG and RSAE with varying ITG turbulence intensity. Here, we illustrate the mechanisms of the regulation of RSAE by ITG and show the feedback from RSAE to ITG. Finally, we summarize the key results of this work and the future plans in section 5.

2. Equilibrium profiles and simulation parameters

Figure 1 shows the magnetic equilibrium and plasma profiles used in the simulations which are selected from DIII-D shot #159243 at 805 ms [9, 51] and reproduced by with the kinetic EFIT code [52] with the on-axis EP temperature $T_{EPa} = 23.6$ keV. The simulations employ a typical reversed magnetic shear configuration with minimal safety factor $q_{min} = 2.94$ near $\rho = 0.5$ (with major radius $R = 1.98$ m on the mid-plane for the low field side), where RSAE are observed in experiments. Here, q represents the ratio of toroidal to poloidal turns of magnetic field lines and ρ is the square root of the toroidal flux normalized by its separatrix value. The on-axis β is $\beta = \beta_e + \beta_i + \beta_f = 1.8\%$. Using eight codes, verification and validation (V&V) of linear simulations [9] have reported observation of RSAE excited by energetic ions with good agreement on linear dispersion among the different codes. The poloidal and radial mode structures of the $n = 4$ RSAE are also found to agree with ECE and ECE imaging [53] measurements. Later linear global GTC simulations [54] find coexistence of lower toroidal mode number n RSAE and higher n ITG driven by thermal plasma pressure gradient in the simulated discharge. The most unstable RSAE near the q_{min} flux surface has a toroidal mode number $n = 4$, with a real frequency $\omega_{4,AE} = -4.28 \times 10^5$ rad s^{-1}, and a growth rate $\gamma_{4,AE} = 3.23 \times 10^4$ s^{-1}. ITG are driven on both side of the q_{min} surface, and the inner ITG that are closer to RSAE have the most unstable mode with $n = 16$, $\omega_{16,ITG} = -8.16 \times 10^4$ rad s^{-1}, and $\gamma_{16,ITG} = 2.2 \times 10^4$ s^{-1}. In GTC, positive sign
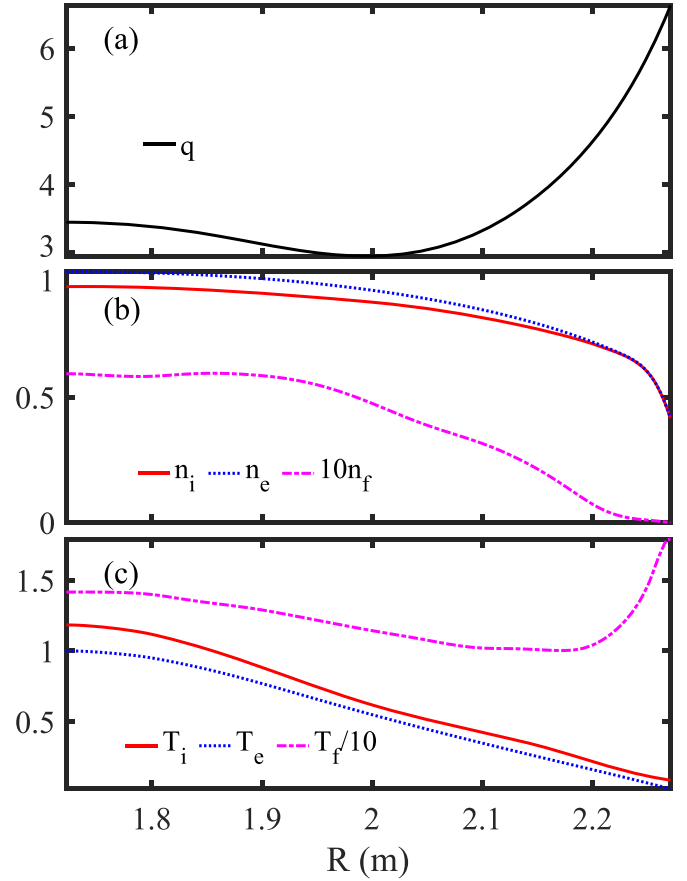

Figure 1. Magnetic equilibrium and plasma profiles from DIII-D shot #159243 at 805 ms. (*a*) q profile. (*b*) Electron n_e, ion n_i and beam ion n_f densities normalized by electron density $n_{ea} = 3.29 \times 10^{19}$ m^{-3} at magnetic axis $R_a = 1.72$ m. (*c*) Electron T_e, ion T_i and beam ion T_f temperatures normalized by on-axis electron temperature $T_{ea} = 1.689$ keV. The radial position of the last closed magnetic flux surface is $R_{edge} = 2.27$ m.

of frequency is defined in electron diamagnetic frequency, so here the minus sign means the real frequency is in ion diamagnetic direction.

In all simulations, an initial Maxwellian distribution is used for all species (electrons, EP and thermal ions), and they are treated using a low noise δf scheme [55]. For the GTC simulation model, EP and thermal ions are described by gyrokinetic model [56], electrons are described by drift kinetic model. Compressible magnetic perturbation [57] and equilibrium current [58] are included for completeness, and the equilibrium pressure profiles of each species are fixed using a model particle and heat source [34]. The radial boundary of the simulation domain is $R = [1.85, 2.15]$ m. Based on the convergence studies, GTC uses a global field-aligned mesh with 32 parallel grid points, which is sufficient to resolve the long parallel wavelength, and 2×10^5 unstructured perpendicular grid points with a grid size $\sim 0.6\rho_i$ to capture short wavelength ITG, where $\rho_i \sim 2.1$ mm is the thermal ion gyroradius. Time step is set to be 2×10^{-5} ms to resolve the high frequency RSAE and the fast electron thermal motion $v_{th,e} \sim 2 \times 10^7$ m s^{-1}. Additionally, a large particle number per cell

6000 is used for each species to minimize the noise. In all simulations, the initial condition is only random noise, and all poloidal m harmonics are included when using Fourier filtering to select specific toroidal modes.

3. Nonlinear simulations of ITG microturbulence

We begin with global nonlinear electrostatic and electromagnetic simulations focusing only on the ITG to investigate the ITG nonlinear dynamics and associated thermal plasma transport. In these simulations, we exclude EP by setting $n_i = n_e$ and keep multiple toroidal modes $n = [0, 25]$ with $k_\theta \rho_i \sim 0.7$ for $n = 25$, where k_θ stands for the poloidal wave number.

Figure 2(*a*) displays the time history of the scalar potential from the electrostatic ITG simulation. Linearly unstable ITG, such as $n = 14$ and 16, are firstly driven. Linearly stable modes, such as $n = 4$ and 5, are then nonlinearly generated after 0.1 ms due to nonlinear mode coupling. Near 0.22 ms, the ITG saturate and maintain a steady state nonlinear phase. Electrostatic ITG simulation with EP is also performed and the EP effects on the thermal plasma are found to be negligible. In the electromagnetic ITG simulation, as shown in figure 2(*b*), linearly stable modes are nonlinearly generated shortly before the saturation of strong unstable modes and saturate at higher levels. Figure 3(*a*) shows that the $n = 1$ ($m = 3$) mode dominates the electromagnetic ITG in the nonlinear phase due to inverse cascading [59]. However, due to the finite β-effect, ITG saturates at lower amplitudes in the electromagnetic simulation than in the electrostatic ITG simulation.

The zonal flows ϕ_z from electrostatic ITG are larger than electromagnetic ITG due to the larger turbulence intensity. However, figure 2 shows that zonal flow shearing rate $\omega_E(R) = -R^2 B_\theta \left(\partial^2 \phi_z / \partial \psi^2 \right)$ possesses similar amplitude in the late nonlinear phase for both electrostatic and electromagnetic ITG, due to the smaller radial wave number k_r of ϕ_Z from electrostatic ITG than the electromagnetic ITG as indicated by figure 4(*b*) that displays the radial profiles of the zonal flow shearing rate $\omega_E(R)$ at $t = 0.6$ ms. Here, $\omega_E(R)$ has been normalized by the linear growth rate $\gamma_{4,AE}$ of the $n = 4$ RSAE, while the root-mean-square value $\omega_E(t)$ in [28] is normalized by $2\pi \gamma_{4,AE}$. For a similar amplitude of zonal flow shearing rate ω_E, a smaller k_r component has a stronger shearing effect on the microturbulence.

Figure 4(*a*) displays the radial profiles of effective thermal ion heat conductivity $\chi_i(R)$, obtained from averaging over the time domain $t = [0.48, 0.72]$ ms of thermal ion heat flux $Q_i(R,t) / \nabla T_i$ as a function of major radius R and time t, for both electrostatic and electromagnetic simulations. The thermal ion heat flux $Q_i(R,t)$ is calculated using the equation,

$$Q_i(R,t) = \int \left(\frac{m_i v_i^2}{2} - \frac{3T_i}{2} \right) v_{dr}(R,t) \, \delta f_i(R,t) \, dv^3,$$

where m_i is the ion mass, v_i is the ion thermal velocity, δf_i is the perturbed ion distribution function, and v_{dr} is the radial
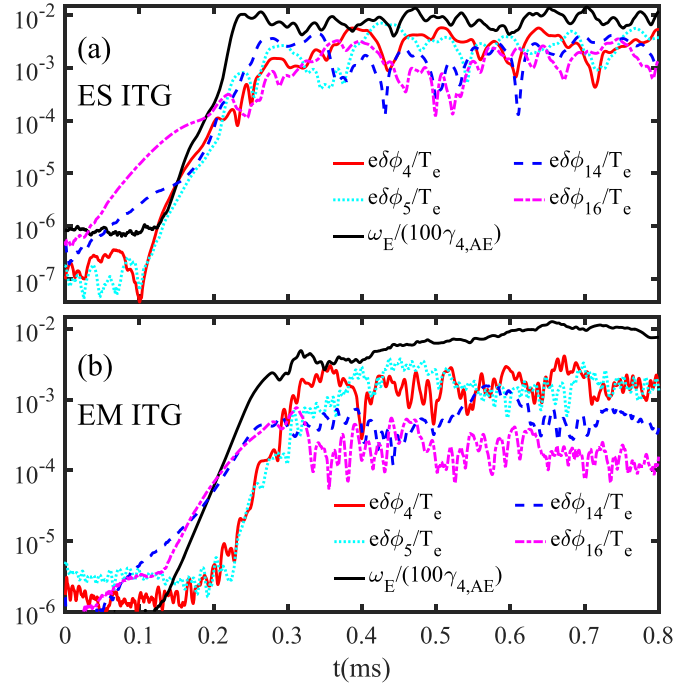

Figure 2. Time history of perturbed electrostatic potential $e\delta\phi_n/T_e$ for selected toroidal n modes on q_{min} flux surface from electrostatic [panel (*a*)] and electromagnetic [panel (*b*)] ITG. The black line represents the normalized zonal flow shearing rate $\omega_E / (100 \gamma_{4,AE})$ which is root-mean-square (rms) value averaged over the radial domain of the major radius $R = [1.95, 2.04]$ m.
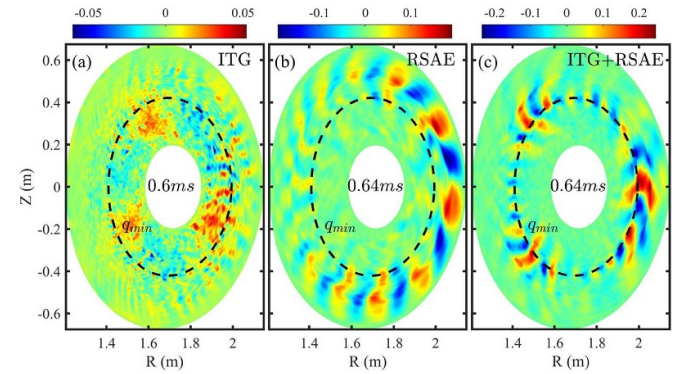

Figure 3. Poloidal contour plot of perturbed electrostatic potential $e\delta\phi/T_e$ at $t = 0.6$ms from electromagnetic ITG simulation [panel (*a*)]. Panel (*b*) shows the poloidal contour plot of $e\delta\phi/T_e$ at $t = 0.64$ms from RSAE simulation, and panel (*c*) shows the poloidal contour plot of $e\delta\phi/T_e$ at $t = 0.64$ ms from simulation coupling ITG and RSAE.

component of gyrocenter drift velocity $\boldsymbol{v}_d$, which includes $\boldsymbol{E} \times \boldsymbol{B}$ drift and magnetic-flutter terms for electromagnetic simulation,

$$\boldsymbol{v}_d = \frac{\boldsymbol{B}_0 \times \nabla \langle \delta\phi \rangle}{B_0^2} + v_{||} \frac{\delta \boldsymbol{B}_\perp}{B_0},$$

with gyro-averaging $<>$, $v_{||}$ the parallel velocity, $\delta \boldsymbol{B}_\perp$ the perpendicular magnetic perturbation, and B_0 the equilibrium magnetic field. In electrostatic simulation, ITG can drive a
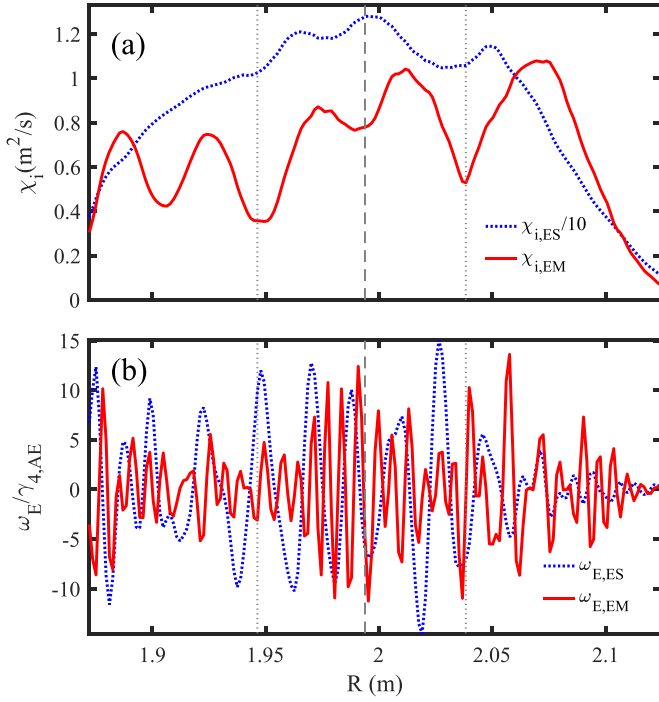
4

Figure 4. Radial structures of effective thermal ion heat conductivity $\chi_i(R)$ [panel (*a*)] and normalized zonal flow shearing rate $\omega_E(R)$ [panel (*b*)] after nonlinear saturation from electrostatic (blue dot) and electromagnetic (red solid) ITG simulations. The vertical gray dot lines from left to right represent the $q = 3$ resonant surfaces at $R = 1.945$ m and $R = 2.038$ m, and the vertical gray dash lines represent the $q_{\min}$ location.

huge thermal ion heat transport. Due to finite β effect, however, it can be reduced by a factor of 10 reaching experimental level of $\sim 1\text{m}^2\text{ s}^{-1}$ in electromagnetic simulation, where the heat flux is dominated by $\boldsymbol{E} \times \boldsymbol{B}$ drift. Moreover, $\chi_i(R)$ in both simulations, especially in the electromagnetic simulation, exhibit a lower value at the specific resonant surfaces $q = 3$ at $R = 1.945$ m and $R = 2.038$ m.

4. Cross-scale coupling between RSAE and ITG

4.1. Regulation of RSAE by ITG

In the simulations coupling ITG microturbulence and meso-scale RSAE, an electromagnetic simulation of the ITG turbulence with EP is initiated by using Fourier filtering to remove all fluctuating fields of the $n = [1, 10]$ RSAE and keeping only the $n = [11, 25]$ ITG and the $n = 0$ zonal mode to provide a background microturbulence. The EP contribution slightly decreases the ITG linear growth rate. The time chosen for launching the RSAE is crucial. Firstly, the launch time should not be too early, since the RSAE needs to be saturated after ITG saturation to investigate the effects of ITG on both linear and nonlinear phase of RSAE. Secondly, the launch time should not be too late, as the filtering of lower n modes $n = [1, 10]$ would truncate the inverse cascading of ITG. Figure 2 has shown that the longer wavelength modes (e.g. $n = 4$ and 5) are marginally stable with very small amplitudes
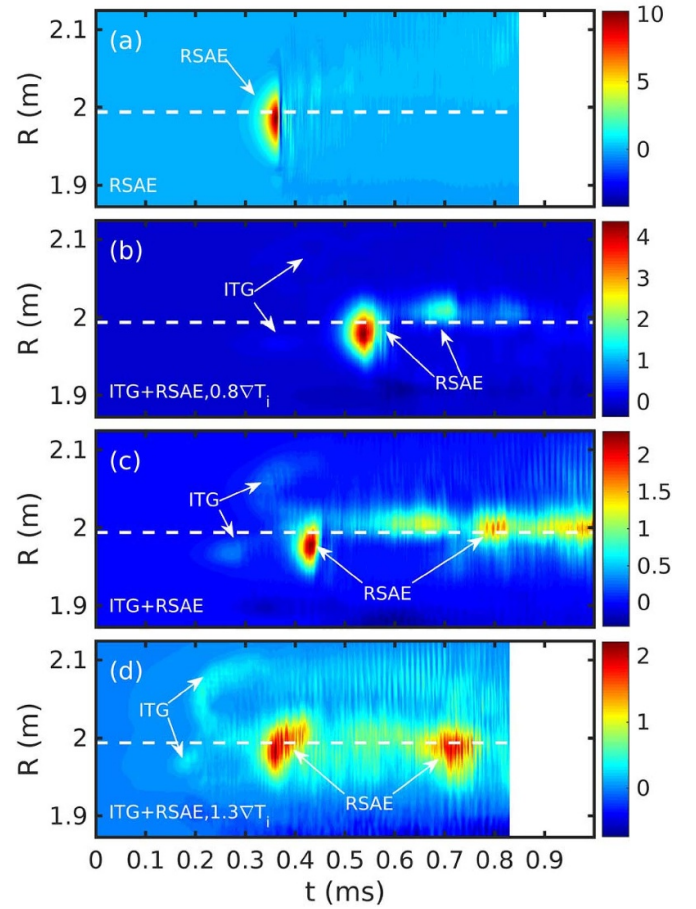

Figure 5. EP effective diffusivity $D_f(R,t) \left(\text{m}^2\text{ s}^{-1}\right)$ as a function of major radius R and time t from single scale RSAE simulation [panel (*a*)] and simulations coupling ITG and RSAE with $0.8\nabla T_i$ [panel (*b*)], original ∇T_i [panel (*c*)], and $1.3\nabla T_i$ [panel (*d*)]. The white dash lines represent q_{min} location and the unit of color bar is $\text{m}^2\text{ s}^{-1}$.

in the early linear phase ($t < 0.2$ ms), so the absence of these long wavelength modes before $t = 0.2$ ms does not affect the ITG saturation at $t \sim 0.3$ ms. Therefore, the RSAE is added at 0.18 ms by allowing the $n = [1, 10]$ modes in the self-consistent simulation.

Figure 5(*c*) illustrates the EP effective diffusivity $D_f(R,t) = \Gamma_f(R,t) / \nabla n_f$, i.e. particle flux normalized by density gradient, as a function of major radius R and time t obtained from simulation coupling ITG and RSAE, where the calculation of $\Gamma_f(R,t)$ in GTC has been described at the end of section 3.1 in [18]. After the initiation of the RSAE, the inner ITG saturates near 0.25 ms and the outer ITG saturates near 0.3 ms. RSAE saturates near 0.43ms with maximal amplitude near the $q_{\min}$ flux surface, and the EP transport driven by the RSAE is much larger than that directly driven by the ITG. After the initial saturation of the RSAE, instead of the quenched nonlinear phase in the single scale RSAE simulation as shown in figure 5(*a*), a quasi-steady state nonlinear phase can be maintained in the coupled simulation. However, unlike the EP transport at the initial saturation of the RSAE, the quasi-steady state EP transport mostly localizes just outside the $q_{\min}$ flux surface. Compared to simulation focusing only on the RSAE, as
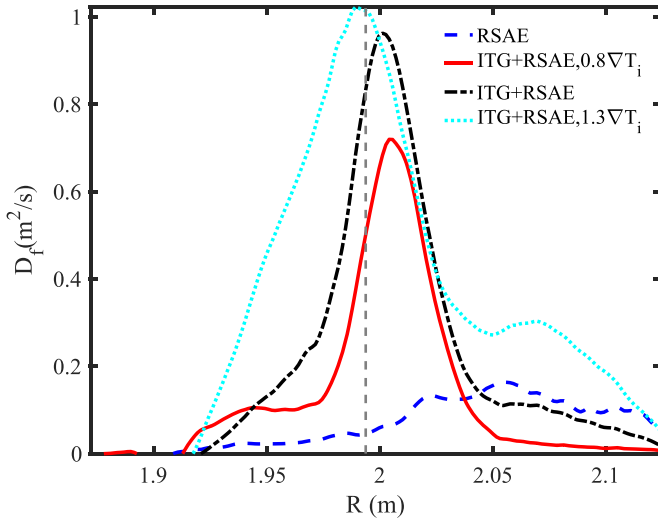
Figure 6. Radial structures of effective EP diffusivity $D_f(R)$ in nonlinear phase from single scale RSAE simulation (blue dash) as well as simulations coupling ITG and RSAE with $0.8\nabla T_i$ (red solid), original ∇T_i (black dot dash), and $1.3\nabla T_i$ (cyan dot). The vertical gray dash line represents the q_{min} location.

Figure 7. Perturbed EP distribution function δf in (P_ζ, λ) phase space with fixed $\mu B_a = 80\,\text{keV}$ at 0.8 ms from single scale RSAE simulation [panel (*a*)] and at 0.83 ms from standard coupled simulation [panel (*b*)]. The black lines represent the dominant linear resonance.

shown in figure 1 of [28], ITG affects the RSAE linear growth, and suppresses mode amplitude and associated EP transport at the initial RSAE saturation, but enhances the quasi-steady EP transport to the experimental level. In addition, near the q_{min} flux surface, quasi-steady RSAE exhibits a regular 2D mode structure with maximal amplitude as shown in figure 3(*c*), instead of the broken RSAE structure in the simulation focusing only on RSAE as shown in figure 3(*b*) where the nonlinear generated TAE outside the q_{min} flux surface has been described in section 5 of [18].

To account for experimental measurement uncertainties, we carry out a sensitivity study of ITG intensity by varying the thermal ion temperature gradient. We reduced the thermal ion temperature gradient by 20% to provide a weaker background microturbulence, as depicted in figure 5(*b*), resulting in a later ITG saturation and a smaller ITG-induced EP transport. Consequently, the effects of suppression at the initial saturation of RSAE and enhancement of EP transport in the nonlinear phase by weaker background ITG are weaker than the standard background ITG. Conversely, we increased the thermal ion temperature gradient by 30% to provide a stronger background microturbulence, as shown in figure 5(*d*), leading to an earlier ITG saturation, and larger ITG-induced EP transport. The stronger ITG strongly suppresses the initial saturation of RSAE, but a second burst can even be observed. As expected, the regulation of the RSAE by a stronger ITG is stronger. We also carry out simulations focusing only on RSAE with $0.8\nabla T_i$ and $1.3\nabla T_i$ and confirm that the slight changes in ∇T_i have little effects on the linear dispersion and nonlinear dynamics of the RSAE in the single scale RSAE simulations.

The time history of effective EP diffusivity $D_f(t)$ has been previously shown in figure 1 of [28] for both single scale RSAE simulation and simulations coupling RSAE and ITG
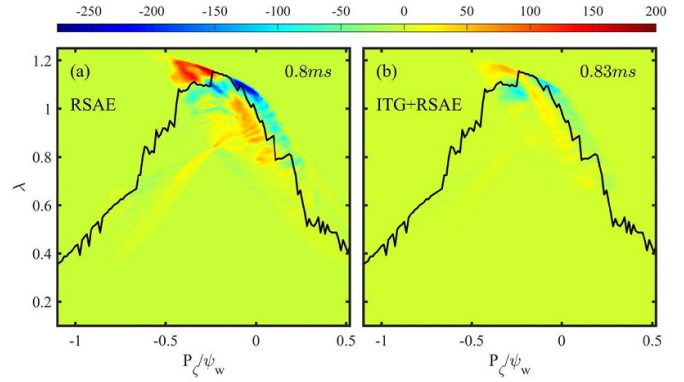
with various ∇T_i. Figure 6 illustrates radial profiles of quasi-steady EP transport $D_f(R)$ obtained by the time average from the start point selected to be right after the RSAE initial saturation to the end of simulation. In the single scale RSAE simulation, the associated EP transport $D_f(R) < 0.2$ m² s⁻¹ is much smaller than the experimental measurement in the entire radial domain. However, in the coupled simulations, the EP transport has the right order of magnitude to interpretive modeling value of 2.5 m² s⁻¹ [60] and mostly localizes just outside the q_{min} flux surface for weaker background microturbulence, while it is observed in a wider radial domain with a larger value for a stronger background microturbulence.

In simulations focusing only on RSAE, the nonlinear dynamics of both RSAE amplitude and EP transport show a large initial burst followed by a quenched nonlinear phase. However, in coupled simulations, the RSAE amplitude and EP transport decrease significantly at the initial saturation, but later increase to experimental levels in the quasi-steady state. Two physical processes may be attributed to maintaining the quasi-steady state AE turbulence in the presence of ITG: first, ITG can scatter the resonant EP nonlinearly trapped by RSAE, and second, ITG can damp zonal flows generated by RSAE.

We first examine the ITG scattering effects on the resonant EP nonlinearly trapped by RSAE through the phase space nonlinear dynamics. Figure 6 in [18] shows that the nonlinearly trapped EP by the RSAE in the simulated discharge consists of both magnetically trapped and passing particles. Figure 7 shows the comparison of EP distribution perturbation δf in the phase space (P_ζ, λ) for a fixed magnetic moment $\mu B_a = 80\,\text{keV}$ between single scale RSAE simulation and standard coupled simulation, where $\lambda = \mu B_a / E$ is the pitch angle and P_ζ is the canonical angular moment normalized by the poloidal magnetic flux at wall ψ_w,

$$P_\zeta = g\frac{m_f}{Z_f B_0}v_{f||} - \psi,$$

with μ the magnetic moment, B_a the on-axis equilibrium magnetic field, E the kinetic energy, g the covariant component of
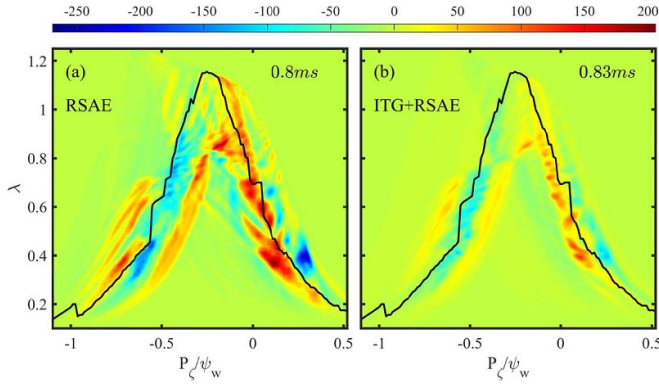
Figure 8. Perturbed EP distribution function δf in (P_ζ, λ) phase space with fixed $\mu B_a = 25\,\text{keV}$ at $0.8\,\text{ms}$ from single scale RSAE simulation [panel (*a*)] and at $0.83\,\text{ms}$ from standard coupled simulation [panel (*b*)]. The black lines represent the dominant linear resonance.

equilibrium magnetic field, ψ the poloidal magnetic flux function, B_0 the equilibrium magnetic field, and m_f, Z_f, $v_{f\parallel}$ the beam ion mass, charge, and parallel velocity, respectively. Instead of the clump-hole structures with large amplitudes dominated by deeply magnetically trapped particles which reduces the drive and quenches the RSAE [61] in the nonlinear phase of the single scale RSAE simulation, we can see the reduction of the amplitude and the shrinking of the EP coherent structures in the presence of background ITG. Specifically, the EP scattering by the ITG restores the EP initial profile and linear drive by reducing the flattening of EP profile in the resonance region.

For another magnetic moment $\mu B_a = 25$ keV where both magnetically passing and trapped particles play an important role in the resonance, ITG has strong scattering effects on both magnetically passing and trapped particles as shown in figure 8. Therefore, the EP scattering by the ITG can be attributed to the maintaining of quasi-steady state AE turbulence.

We then examine the zonal structures in the absence and presence of background ITG to investigate the ITG effects on the zonal flows generated by the RSAE. The zonal structures in nonlinear phase presented in figures 9(*c*) and (*e*) are selected from simulation focusing only on RSAE and standard coupled simulation when zonal flow shearing rate reaches its minimum value after the RSAE saturation, as shown in figure 1 of [28] where the damping of the zonal flow shearing rate is observed in the presence of background ITG. We can find that zonal flows are mostly generated by thermal plasma in both simulations. And the amplitude of zonal component of thermal ion δN_{i00} and electron δN_{e00} in the coupled simulation are smaller than the single scale RSAE simulation but larger than the single scale ITG simulation as shown in figure 9(*a*). Particularly, a reduced amplitude of δN in the entire radial domain is observed in the coupled simulation due to the ITG diffusion.

Figures 9(*d*) and (*f*) show, respectively, the spectrum of zonal structures from simulation focusing only on the RSAE and standard coupled simulation. In both simulations, the spectrum of δN_{f00} peaks at long wavelength region with

$k_r\rho_i = 0.11$ which is similar to the poloidal spectrum of $n = 4$ RSAE with $k_\theta\rho_i = 0.11$ near $q_{\min}$ flux surface. In the single scale RSAE simulation as shown in figure 9(*d*), δN_{i00} and δN_{e00} have a wide spectrum with $0.78 < k_r\rho_i < 1.55$, and the long wavelength component mostly locate near the $q_{\min}$ flux surface. In the presence of background ITG as shown in figure 9(*f*), however, the spectra of δN_{i00} and δN_{e00} are narrowed down to $0.92 < k_r\rho_i < 1.32$, where the long wavelength component with $0.6 < k_r\rho_i < 0.71$ and smaller amplitude mostly comes from the oscillation near $R = 2.04\,\text{m}$ and is similar to the single scale ITG simulation as shown in figure 9(*b*). The reduction of amplitude of zonal structures, especially for the low k_r components that are more effective to suppress the RSAE, leads to the weaker zonal flow effects on the RSAE in the coupled simulation than in the simulation focusing only on the RSAE.

4.2. Effects of RSAE on ITG

We now study the effects of the RSAE on the ITG. Figure 10 shows thermal ion effective heat conductivity $\chi_i(R,t)$, i.e. heat flux $Q_i(R,t)/\nabla T_i$ normalized by the temperature gradient, as a function of major radius R and time t in the nonlinear phase from simulations focusing on, respectively, only electromagnetic ITG, only RSAE, and coupled ITG and RSAE. In the simulation focusing only on the electromagnetic ITG (figure 10(*a*)), ITG on both sides of the $q_{\min}$ flux surface spread across the entire radial domain, resulting in the quasi-steady state outward thermal ion heat transport in nonlinear phase. However, heat flux drops to a lower value near the $q = 3$ resonant surfaces. In the simulation focusing only on the RSAE (figure 10(*b*)), the inward and outward thermal ion heat transport driven by the RSAE has a similar amplitude to that driven by the ITG, and the oscillation frequency of the heat flux direction is the RSAE frequency outside $R = 1.9\,\text{m}$. Inside $R = 1.9\,\text{m}$, however, the heat flux is always outward which may be driven by the coexistence of ITG and RSAE for $10 \le n \le 12$ in the simulated discharge [54]. In the simulation coupling the ITG and RSAE as shown in figure 10(*c*), thermal ion heat flux direction also oscillates with the RSAE frequency except for the locations near the $q = 3$ surfaces and $R < 1.9\,\text{m}$. Thermal ion heat flux exhibits both inward and outward directions near the $q_{\min}$ flux surface, but is almost outward away from the $q_{\min}$ flux surface. Averaging over the time domain in the nonlinear phase gives the radial profiles of effective thermal ion heat conductivity $\chi_i(R)$ as shown in figure 11(*a*). We can find that the inward and outward thermal ion heat flux leads to a small effective thermal ion heat conductivity $\chi_i(R) \sim 0$ outside $R = 1.9\,\text{m}$ in the simulation focusing only on the RSAE. Compared with χ_i from the single scale electromagnetic ITG simulation, the effective thermal ion heat conductivity is reduced by more than a factor of 2 in the simulation coupling ITG and RSAE.

Figure 11(*b*) shows the radial profiles of zonal flow shearing rate $\omega_E(R)$ [62] from simulations focusing on, respectively, only electromagnetic ITG, only RSAE, and coupled ITG and RSAE. The $\omega_E(R)$ from single scale RSAE simulation has much larger amplitude but smaller k_r than the coupled
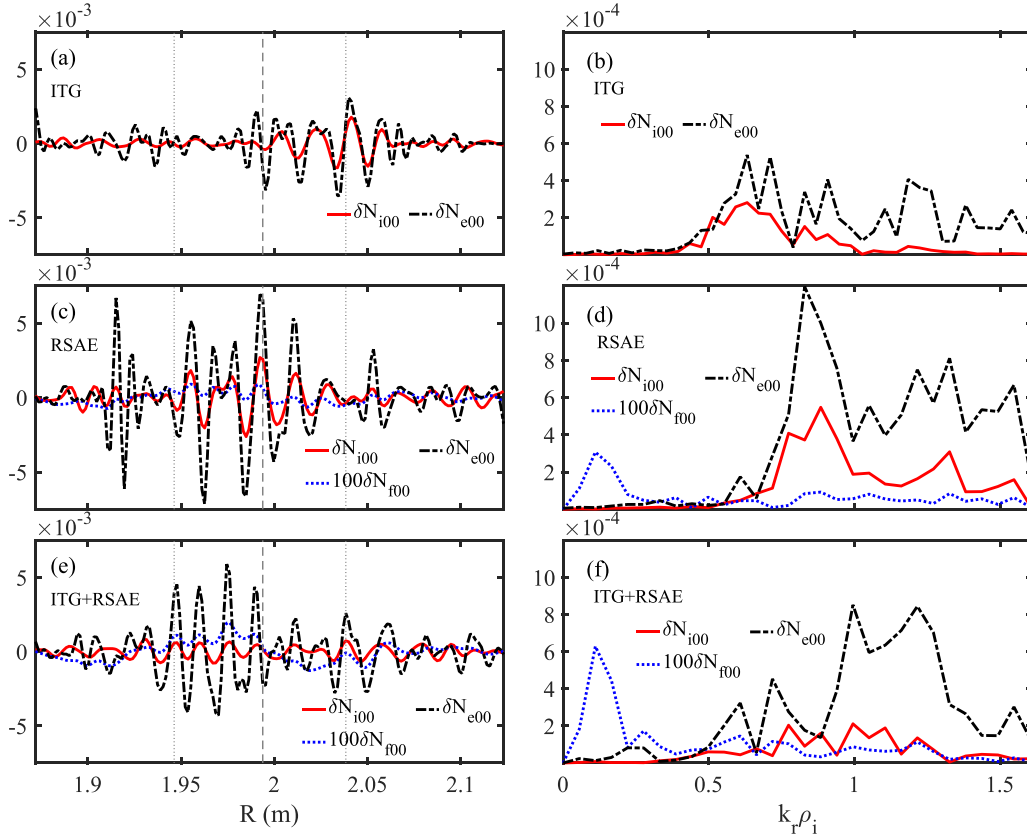
Figure 9. Radial profiles [panel (*a*), (*c*), (*e*)] and spectra [panel (*b*), (*d*), (*f*)] of gyrocenter zonal density [thermal ion δN_{i00} (red solid), and electron δN_{e00} (black dot dash), EP δN_{f00} (blue dot)], where the amplitude of δN_{f00} has been amplified by 100 times. Panel (*a*) and (*b*) are selected from single scale electromagnetic ITG simulation at $t = 0.6$ ms. Panel (*c*) and (*d*) are selected from single scale RSAE simulation at $t = 0.64$ ms, where higher k_r components of δN_{e00} with $k_r \rho_i > 2$ corresponding to the oscillation near $R = 1.92$ m as shown in panel (*c*) have been cut off, since it is far away from RSAE location. Panel (*e*) and (*f*) are selected from standard coupled simulation at $t = 0.64$ ms. The vertical gray dot lines represent the $q = 3$ resonant surfaces at $R = 1.945$ m and $R = 2.038$ m, and the vertical gray dash lines represent the q_{min} location.

simulation outside the $R = 1.945$ m domain. Within the radial domain $R = [1.94, 1.98]$ m, $\omega_E(R)$ from the coupled simulation is larger than that from the single scale ITG simulation, resulting in a small $\chi_i(R)$ in this radial domain. The larger zonal flows are mostly generated by the RSAE [28], but the EP effects may also enhance the generation of the zonal flows by the ITG [63]. Away from $R = [1.94, 1.98]$ m, however, there is no significant enhancement of the $\omega_E(R)$ in the coupled simulation, and the reduction of the time-averaged effective heat conductivity $\chi_i(R)$ of more than a factor of 2 is mostly caused by the oscillation of the thermal ion heat flux direction with RSAE frequency. For the thermal ion heat flux at the specific $q = 3$ resonant surfaces in the coupled simulation, the reduction of $\chi_i(R)$ at $R = 1.945$ m is due to the larger $\omega_E(R)$, while the almost unchanged $\omega_E(R)$ is accompanied by the unchanged $\chi_i(R)$ at the $R = 2.038$ m. Therefore, both the stronger zonal flows generated by the RSAE and the oscillation of the thermal ion heat flux direction can be attributed to the reduction of the thermal ion heat transport in the coupled simulation. Similarly, zonal flows generated by the fishbone instability are expected to suppress the microturbulence in a recent GTC simulation of another DIII-D experiment [64].

In figure 11(*a*), the blue line represents the $\chi_i(R)$ calculated by the Kick model [65] for TRANSP code from power balance, where the kick probabilities are provided by the experimentally measured Alfven eigenmodes [60]. Compared with the blue line, the $\chi_i(R)$ from the standard GTC coupled simulation is too low.

However, the agreement becomes better within the radial domain of two $q = 3$ locations when we consider a slightly stronger background ITG turbulence by increasing the ion temperature gradient by 30%, which lies within the experimental uncertainty. In the simulation focusing only on electromagnetic ITG, thermal ion heat flux driven by the stronger ITG is stronger, as shown in figure 12, and $\chi_i(R)$ also drops to a lower value at the same resonant surfaces, compared with the red solid line in figure 11(*a*). In the coupled simulation with the stronger ITG, the reduction of $\chi_i(R)$ only happens outside the q_{min} surface and is not as much as that in the standard coupled simulation, as shown in the black dot dash line of figure 11(*a*). For the zonal flow shearing rate $\omega_E(R)$ in the simulations focusing only on electromagnetic ITG, figures 11(*b*) and 12(*b*) show that the standard ITG and stronger ITG have similar $\omega_E(R)$. In the coupled simulation with stronger ITG, however, $\omega_E(R)$ is smaller than that in the
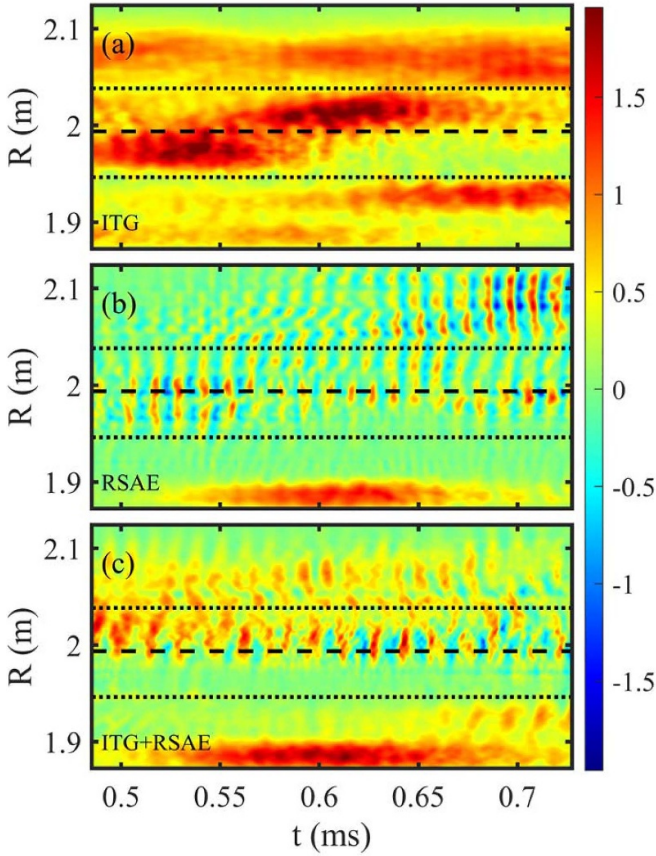
Figure 10. Thermal ion effective heat conductivity $\chi_i(R,t)$ $\left(\mathrm{m}^2\,\mathrm{s}^{-1}\right)$ as a function of major radius R and time t from single scale electromagnetic ITG simulation [panel (*a*)], single scale RSAE simulation [panel (*b*)], and standard coupled simulation [panel (*c*)]. The positive and negative values represent outward and inward transport. The black dot lines represent the $q = 3$ resonant surfaces at $R = 1.945\,\mathrm{m}$ and $R = 2.038\,\mathrm{m}$, and the black dashed lines represent $q_{\min}$ location.

standard coupled simulation except for the resonant surface $q = 3$ at $R = 2.038\,\mathrm{m}$. Accordingly, compared with the simulation focusing only on the stronger electromagnetic ITG, there is no significant enhancement of $\omega_E(R)$ in the presence of the RSAE except for at the resonant surface $q = 3$. The significant increase of $\omega_E(R)$ near the resonant surface leads to a great reduction of $\chi_i(R)$ near $R = 2.038\,\mathrm{m}$ as shown in figure 12(*a*). Away from $R = 2.038\,\mathrm{m}$, the reduction of $\chi_i(R)$ in the coupled simulation is mostly caused by the oscillation of the thermal ion heat flux direction with RSAE frequency. The smaller reduction of $\chi_i(R)$ and enhancement of $\omega_E(R)$ in the coupled simulation with $1.3\nabla\mathrm{T}_i$ indicates that the RSAE effects on the stronger ITG are weaker.

5. Discussion

We perform global nonlinear gyrokinetic simulations using equilibrium and plasma profiles from the DIII-D shot #159243 to investigate the cross-scale interaction between meso-scale RSAE and ITG microturbulence. GTC simulations find:
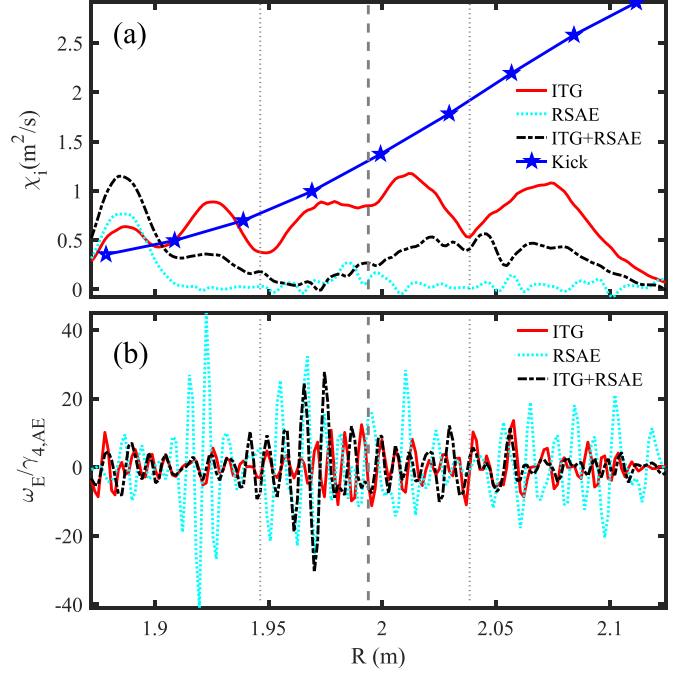

Figure 11. Radial profiles of effective thermal ion heat conductivity $\chi_i(R)$ [panel (*a*)] from GTC simulations with original ∇T_i [single scale electromagnetic ITG simulation (red solid), single scale RSAE simulation (cyan dot), and coupled simulation (black dot dash)] and the reduced model (blue). Panel (*b*) shows the radial profile of normalized zonal flow shearing rate from single scale electromagnetic ITG simulation (red solid) at 0.6 ms, single scale RSAE simulation (cyan dot) at 0.64 ms, and standard coupled simulation (black dot dash) at 0.64 ms. The vertical gray dot lines represent the $q = 3$ resonant surfaces at $R = 1.945\,\mathrm{m}$ and $R = 2.038\,\mathrm{m}$, and the vertical gray dash lines represent the $q_{\min}$ location.

1. In simulations focusing only on ITG, finite β effect greatly reduces thermal ion heat transport.

2. In this simulation coupling ITG and RSAE, EP scattering effects and damping of zonal flows due to ITG can be contributed to the regulation of RSAE by ITG. In turn, the stronger zonal flows generated by the RSAE and the RSAE frequency modulation of the ITG-induced thermal ion heat transport can be attributed to the RSAE effects on the ITG.

3. For a stronger background ITG, the regulation of the RSAE by the ITG is stronger, while the effects of the RSAE on the ITG are weaker.

4. The RSAE amplitude δT_e and electron density fluctuation δn_e spectra in the quasi-steady state ITG-RSAE turbulence qualitatively agree with experimental measures (table 1).

Self-consistent GTC simulations reported in [18, 28] and the present work, systematically reveal the limitation of single scale simulations and the critical role of cross-scale coupling on the EP-thermal plasmas nonlinear dynamics. The agreements quantitively validate the GTC nonlinear electromagnetic simulation model and ensure that the GTC code can predict α-particle confinement in future burning plasmas. However, table 1 shows the discrepancy of EP and bulk ion
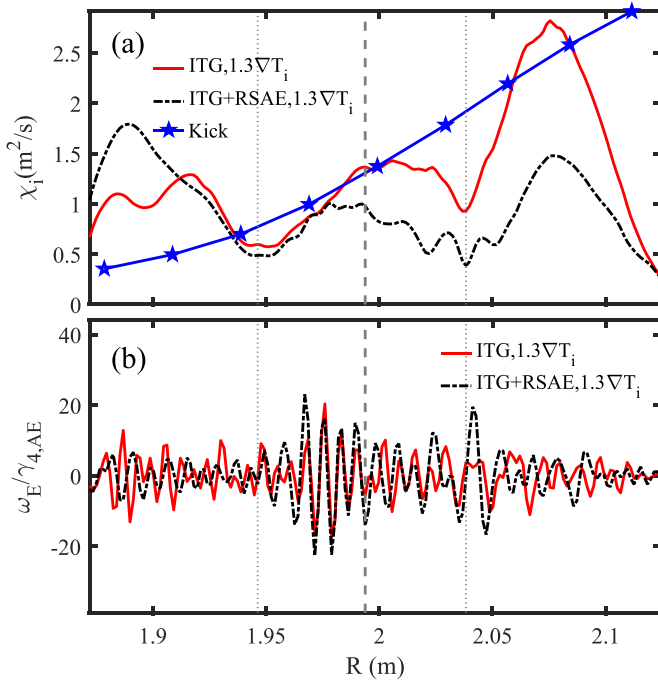
Figure 12. Radial profiles of effective thermal ion heat conductivity $\chi_i(R)$ [panel (*a*)] from GTC simulations with $1.3\nabla T_i$ [single scale electromagnetic ITG simulation (red solid) and coupled simulation (black dot dash)] and reduced model (blue). Panel (*b*) shows the radial profile of normalized zonal flow shearing rate from single scale electromagnetic ITG simulation (red solid) and coupled simulation (black dot dash). The vertical gray dot lines represent the $q = 3$ resonant surfaces at $R = 1.945$ m and $R = 2.038$ m, and the vertical gray dash lines represent the $q_{\min}$ location.

Table 1. Comparisons of standard coupled simulation results with DIII-D experimental measurements near $q_{\min}$. The coefficient C is defined as $C = |\text{GTC} - \exp| / \exp$.

	$D_f \left(\text{m}^2\,\text{s}^{-1}\right)$	$\chi_i \left(\text{m}^2\,\text{s}^{-1}\right)$	δT_e (eV)	$k_\theta \rho_i$ of δn_e
GTC	0.96	0.35	5.5	0.38
Exp	2.5	1.3	4.8	< 0.5
C	61.6%	73.1%	14.6%	24%

transport between the standard GTC coupled simulation and experimental value is still too large. The approximations, such as the isotropic Maxwellian EP distribution and the fixed profiles, may lead to some difference in the simulation results. Moreover, compared with intermittent AE activity in experiments, the short simulated time does not provide a complete description of the EP transport.

In the future, our plans are the following:

1. Effects of experimental EP distribution and evolved profiles on the cross-scale coupling between RSAE and ITG will be explored, using the simulated equilibrium and profiles.
2. Coupled simulations using equilibrium and profiles from other machines will be conducted to validate the GTC simulation model.

3. Predication of α-particle confinement in burning fusion plasmas will be made.

ORCID iDs

P. Liu ⓘ https://orcid.org/0000-0002-6739-3684
X. Wei ⓘ https://orcid.org/0000-0001-7486-0407
W.W Heidbrink ⓘ https://orcid.org/0000-0002-6942-8043
G.J. Choi ⓘ https://orcid.org/0000-0003-0044-1650
J.H. Nicolau ⓘ https://orcid.org/0000-0003-1470-1820
W. Zhang ⓘ https://orcid.org/0000-0002-7136-2119

References

[1] Fasoli A. *et al* 2007 Chapter 5: Physics of energetic ions *Nucl. Fusion* **47** S264
[2] Breizman B.N. and Sharapov S.E. 2011 Major minority: energetic particles in fusion plasmas *Plasma Phys. Control. Fusion* **53** 054001
[3] Gorelenkov N.N., Pinches S.D. and Toi K. 2014 Energetic particle physics in fusion research in preparation for burning plasma experiments *Nucl. Fusion* **54** 125001
[4] Heidbrink W.W. and White R.B. 2020 Mechanisms of energetic-particle transport in magnetically confined plasmas *Phys. Plasmas* **27** 030901
[5] Heidbrink W.W. 2008 Basic physics of Alfvén instabilities driven by energetic particles in toroidally confined plasmas *Phys. Plasmas* **15** 055501
[6] Chen L. and Zonca F. 2016 Physics of Alfvén waves and energetic particles in burning plasmas *Rev. Mod. Phys.* **88** 015008
[7] Todo Y. 2019 Introduction to the interaction between energetic particles and Alfven eigenmodes in toroidal plasmas *Rev. Mod. Plasma Phys.* **3** 1
[8] Spong D.A., Bass E.M., Deng W., Heidbrink W.W., Lin Z., Tobias B., Van Zeeland M.A., Austin M.E., Domier C.W. and Luhmann N.C. 2012 Verification and validation of linear gyrokinetic simulation of Alfvén eigenmodes in the DIII-D tokamak *Phys. Plasmas* **19** 082511
[9] Taimourzadeh S. *et al* 2019 Verification and validation of integrated simulation of energetic particles in fusion plasmas *Nucl. Fusion* **59** 066006
[10] Spong D.A., Carreras B.A. and Hedrick C.L. 1994 Nonlinear evolution of the toroidal Alfvén instability using a gyrofluid model* *Phys. Plasmas* **1** 1503
[11] Zhang H.S., Lin Z. and Holod I. 2012 Nonlinear frequency oscillation of Alfvén eigenmodes in fusion plasmas *Phys. Rev. Lett.* **109** 025001

Q4
Q5

Q6
Q7

[12] Wang X.Q. *et al* 2021 Nonlinear simulations of energetic particle-driven instabilities interacting with Alfvén continuum during frequency chirping *Plasma Phys. Control. Fusion* **63** 015004

[13] Todo Y., Berk H.L. and Breizman B.N. 2010 Nonlinear magnetohydrodynamic effects on Alfvén eigenmode evolution and zonal flow generation *Nucl. Fusion* **50** 084016

[14] Lang J., Fu G.-Y. and Chen Y. 2010 Nonlinear simulation of toroidal Alfvén eigenmode with source and sink *Phys. Plasmas* **17** 042309

[15] Chen Y., Fu G.Y., Collins C., Taimourzadeh S. and Parker S.E. 2018 Zonal structure effect on the nonlinear saturation of reverse shear Alfven eigenmodes *Phys. Plasmas* **25** 032304

[16] Vlad G., Briguglio S., Fogaccia G., Fusco V., Di Troia C., Giovannozzi E., Wang X. and Zonca F. 2018 Single- n versus multiple- n simulations of Alfvénic modes *Nucl. Fusion* **58** 082020

[17] Biancalani A., Bottino A., Lauber P., Mishchenko A. and Vannini F. 2020 Effect of the electron redistribution on the nonlinear saturation of Alfvén eigenmodes and the excitation of zonal flows *J. Plasma Phys.* **86** 825860301

[18] Liu P., Wei X., Lin Z., Brochard G., Choi G.J. and Nicolau J.H. 2023 Nonlinear gyrokinetic simulations of reversed shear Alfven eigenmodes in DIII-D tokamak *Rev. Mod. Plasma Phys.* **7** 15

[19] Bass E.M. and Waltz R.E. 2010 Gyrokinetic simulations of mesoscale energetic particle-driven Alfvénic turbulent transport embedded in microturbulence *Phys. Plasmas* **17** 112319

[20] Citrin J., Jenko F., Mantica P., Told D., Bourdelle C., Garcia J., Haverkort J.W., Hogeweij G.M.D., Johnson T. and Pueschel M.J. 2013 Nonlinear stabilization of tokamak microturbulence by fast ions *Phys. Rev. Lett.* **111** 155001

[21] Zonca F., Chen L., Briguglio S., Fogaccia G., Vlad G. and Wang X. 2015 Nonlinear dynamics of phase space zonal structures and energetic particle physics in fusion plasmas *New J. Phys.* **17** 013052

[22] Duarte V.N., Berk H.L., Gorelenkov N.N., Heidbrink W.W., Kramer G.J., Nazikian R., Pace D.C., Podestà M., Tobias B.J. and Van Zeeland M.A. 2017 Prediction of nonlinear evolution character of energetic-particle-driven instabilities *Nucl. Fusion* **57** 054001

[23] Di Siena A., Görler T., Poli E., Navarro A.B., Biancalani A. and Jenko F. 2019 Electromagnetic turbulence suppression by energetic particle driven modes *Nucl. Fusion* **59** 124001

[24] Gorelenkov N.N. and Duarte V.N. 2021 Microturbulence-mediated route for energetic ion transport and Alfvénic mode amplitude oscillations in tokamaks *Phys. Lett.* A **386** 126944

[25] Biancalani A. *et al* 2021 Gyrokinetic investigation of Alfvén instabilities in the presence of turbulence *Plasma Phys. Control. Fusion* **63** 065009

[26] Garcia J. 2022 Electromagnetic and fast ions effects as a key mechanism for turbulent transport suppression at JET *Plasma Phys. Control. Fusion* **64** 104002

[27] Chen L., Qiu Z. and Zonca F. 2022 On scattering and damping of toroidal Alfvén eigenmode by drift wave turbulence *Nucl. Fusion* **62** 094001

[28] Liu P., Wei X., Lin Z., Brochard G., Choi G.J., Heidbrink W.W., Nicolau J.H. and McKee G.R. 2022 Regulation of Alfvén eigenmodes by microturbulence in fusion plasmas *Phys. Rev. Lett.* **128** 185001

[29] Horton W. 1999 Drift waves and transport *Rev. Mod. Phys.* **71** 735

[30] Chen L. and Zonca F. 2012 Nonlinear excitations of zonal structures by toroidal Alfvén eigenmodes *Phys. Rev. Lett.* **109** 145002

[31] Qiu Z., Chen L. and Zonca F. 2016 Effects of energetic particles on zonal flow generation by toroidal Alfvén eigenmode *Phys. Plasmas* **23** 090702

[32] Choi G.J., Diamond P.H. and Hahm T.S. 2024 On how fast ions enhance the regulation of drift wave turbulence by zonal flows *Nucl. Fusion* **64** 016029

[33] Lin Z., Hahm T.S., Lee W.W., Tang W.M. and White R.B. 1998 Turbulent transport reduction by zonal flows: massively parallel simulations *Science* **281** 1835

[34] Lin Z., Ethier S., Hahm T.S. and Tang W.M. 2002 Size scaling of turbulent transport in magnetically confined plasmas *Phys. Rev. Lett.* **88** 195004

[35] Lin Z., Holod I., Chen L., Diamond P.H., Hahm T.S. and Ethier S. 2007 Wave-particle decorrelation and transport of anisotropic turbulence in collisionless plasmas *Phys. Rev. Lett.* **99** 265003

[36] Zhang W., Lin Z. and Chen L. 2008 Transport of energetic particles by microturbulence in magnetized plasmas *Phys. Rev. Lett.* **101** 095001

[37] Xiao Y. and Lin Z. 2009 Turbulent transport of trapped-electron modes in collisionless plasmas *Phys. Rev. Lett.* **103** 085004

[38] Wang H.Y., Holod I., Lin Z., Bao J., Fu J.Y., Liu P.F., Nicolau J.H., Spong D. and Xiao Y. 2020 Global gyrokinetic particle simulations of microturbulence in W7-X and LHD stellarators *Phys. Plasmas* **27** 082305

[39] Nicolau J.H., Choi G., Fu J., Liu P., Wei X. and Lin Z. 2021 Global gyrokinetic simulation with kinetic electron for collisionless damping of zonal flow in stellarators *Nucl. Fusion* **61** 126041

[40] Fu J.Y., Nicolau J.H., Liu P.F., Wei X.S., Xiao Y. and Lin Z. 2021 Global gyrokinetic simulation of neoclassical ambipolar electric field and its effects on microturbulence in W7-X stellarator *Phys. Plasmas* **28** 062309

[41] McClenaghan J., Lin Z., Holod I., Deng W. and Wang Z. 2014 Verification of gyrokinetic particle simulation of current-driven instability in fusion plasmas. I. Internal kink mode *Phys. Plasmas* **21** 122519

[42] Brochard G. *et al* 2022 Verification and validation of linear gyrokinetic and kinetic-MHD simulations for internal kink instability in DIII-D tokamak *Nucl. Fusion* **62** 036021

[43] Wang Z., Lin Z., Holod I., Heidbrink W.W., Tobias B., Van Zeeland M. and Austin M.E. 2013 Radial localization of toroidicity-induced Alfvén eigenmodes *Phys. Rev. Lett.* **111** 145003

[44] Choi G.J., Liu P., Wei X.S., Nicolau J.H., Dong G., Zhang W.L., Lin Z., Heidbrink W.W. and Hahm T.S. 2021 Gyrokinetic simulation of low-frequency Alfvénic modes in DIII-D tokamak *Nucl. Fusion* **61** 066007

[45] Heidbrink W.W., Park J.M., Murakami M., Petty C.C., Holcomb C. and Van Zeeland M.A. 2009 Evidence for fast-ion transport by microturbulence *Phys. Rev. Lett.* **103** 175001

[46] Hauff T., Pueschel M.J., Dannert T. and Jenko F. 2009 Electrostatic and magnetic transport of energetic ions in turbulent plasmas *Phys. Rev. Lett.* **102** 075004

[47] Albergante M., Graves J.P., Fasoli A., Jenko F. and Dannert T. 2009 Anomalous transport of energetic particles in ITER relevant scenarios *Phys. Plasmas* **16** 112301

[48] Pueschel M.J., Jenko F., Schneller M., Hauff T., Günter S. and Tardini G. 2012 Anomalous diffusion of energetic particles: connecting experiment and simulations *Nucl. Fusion* **52** 103018

[49] Austin M.E. and Lohr J. 2003 Electron cyclotron emission radiometer upgrade on the DIII-D tokamak *Rev. Sci. Instrum.* **74** 1457

[50] Gupta D.K., Fonck R.J., McKee G.R., Schlossberg D.J. and Shafer M.W. 2004 Enhanced sensitivity beam emission

spectroscopy system for nonlinear turbulence measurements *Rev. Sci. Instrum.* **75** 3493

[51] Collins C.S., Heidbrink W., Austin M., Kramer G., Pace D., Petty C., Stagner L., Van Zeeland M., White R. and Zhu Y. 2016 Observation of critical-gradient behavior in Alfvén-eigenmode-induced fast-ion transport *Phys. Rev. Lett.* **116** 095001

[52] Lao L.L., John H.S., Stambaugh R.D., Kellman A.G. and Pfeiffer W. 1985 Reconstruction of current profile parameters and plasma shapes in tokamaks *Nucl. Fusion* **25** 1611

[53] Tobias B. *et al* 2010 Commissioning of electron cyclotron emission imaging instrument on the DIII-D tokamak and first data *Rev. Sci. Instrum.* **81** 10D928

[54] Wang H., Liu P., Lin Z. and Zhang W. 2021 Linear gyrokinetic simulations of reversed shear Alfvén eigenmodes and ion temperature gradient modes in DIII-D tokamak *Plasma Sci. Technol.* **23** 015101

[55] Parker S.E. and Lee W.W. 1993 A fully nonlinear characteristic method for gyrokinetic simulation *Phys. Fluids* B **5** 77

[56] Brizard A.J. and Hahm T.S. 2007 Foundations of nonlinear gyrokinetic theory *Rev. Mod. Phys.* **79** 421

[57] Dong G., Bao J., Bhattacharjee A., Brizard A., Lin Z. and Porazik P. 2017 Gyrokinetic particle simulations of the effects of compressional magnetic perturbations on drift-Alfvenic instabilities in tokamaks *Phys. Plasmas* **24** 081205

[58] Deng W., Lin Z. and Holod I. 2012 Gyrokinetic simulation model for kinetic magnetohydrodynamic processes in magnetized plasmas *Nucl. Fusion* **52** 023005

[59] Tennekes H. and Lumley J.L. 1972 *A First Course in Turbulence* (MIT Press)

[60] Heidbrink W.W., Collins C.S., Podestà M., Kramer G.J., Pace D.C., Petty C.C., Stagner L., Van Zeeland M.A., White R.B. and Zhu Y.B. 2017 Fast-ion transport by Alfvén eigenmodes above a critical gradient threshold *Phys. Plasmas* **24** 056109

[61] Berk H.L., Breizman B.N. and Ye H. 1992 Scenarios for the nonlinear evolution of alpha-particle-induced Alfvén wave instability *Phys. Rev. Lett.* **68** 3563

[62] Hahm T.S., Beer M.A., Lin Z., Hammett G.W., Lee W.W. and Tang W.M. 1999 Shearing rate of time-dependent E×B flow *Phys. Plasmas* **6** 922

[63] Hahm T.S., Choi G.J., Park S.J. and Na Y.-S. 2023 Fast ion effects on zonal flow generation: a simple model *Phys. Plasmas* **30** 072501

[64] Brochard G. *et al* 2024 Saturation of fishbone instability by self-generated zonal flows in tokamak plasmas *Phys. Rev. Lett.* **132** 075101

[65] Podestà M., Gorelenkova M. and White R.B. 2014 A reduced fast ion transport model for the tokamak transport code TRANSP *Plasma Phys. Control. Fusion* **56** 055003